Nano-Micro Letters

e-ISSN 2150-5551
CN 31-2103/TB

ARTICLE

https://doi.org/10.1007/s40820-026-02117-8

Cite as
Nano-Micro Lett.
(2026) 18:263

Received: 8 November 2025
Accepted: 19 January 2026

Graphene-Skinned Fiber with Fine-Tunable Electrical Resistance via Radical and Substrate Engineering for Electromagnetic-Thermal Fabric

Jie Liang[1], Zhaochen Li[1], Fang Ye[1] ✉, Yuchen Cao[1], Yi An[1], Xiaomeng Fan[1] ✉, Qiang Song[1] ✉

HIGHLIGHTS

- The composition of $C_1/C_2/C_6$ radicals is strategically regulated by temperature, dictating the growth of either defective or highly textured graphene microstructures.
- A synergistic strategy involving radical manipulation and substrate effect via methanol- chemical vapor deposition enables precise control of graphene microstructure, allowing fine tuning of sheet resistance from 26 to 150 Ω sq^{-1}.
- Laser-patterned band-pass frequency selective surface and a sandwich structure synergistically achieve excellent broadband wave transmission (7.29 GHz) and effective Joule heating (72 °C).

ABSTRACT This work demonstrates a radical-manipulation strategy for synthesizing graphene (Gr)-skinned SiO_2 fabric via low-pressure chemical vapor deposition using methanol precursor. Controlled pyrolysis at high temperature regulated $C_1/C_2/C_6$ radical ratios, enabling microstructure engineering. Substrate effects governed bilayer evolution. SiO_2 imposed lower adsorption energy of C_1 and higher diffusion barriers of radical compared to Gr, promoting edge defects in subsurface G1-type Gr layers, whereas reduced substrate constraints facilitated low-defect G2-type Gr growth on top of G1-type Gr. Synergistic control of gas-phase kinetics and substrate dynamics enabled fine-tunable sheet resistance (26–150 Ω sq^{-1}), establishing Gr-skinned fibers as multifunctional platforms for integrated electromagnetic-thermal management systems. When addressing the needs of electromagnetic communication and electrothermal deicing, laser-etched band-pass frequency selective surface structures of Gr-skinned fabric were fabricated to achieve electromagnetic wave (EMW) transmittance while maintaining Joule heating capability. A sandwich structure was prepared by laminating the Gr-skinned fabric with EMW transparent sheets exhibiting voltage-dependent transmittance, simultaneously sustaining broadband transmission and effective heating. This work demonstrates a strategy to mitigate the longstanding conductivity-EMW transparency trade-off in Gr-functionalized fibers through a multiscale engineering that coordinates microscopic structural regulation with macroscopic patterning, thereby unlocking next-generation smart composites for 5G/6G wearables, aerospace radomes, and beyond.

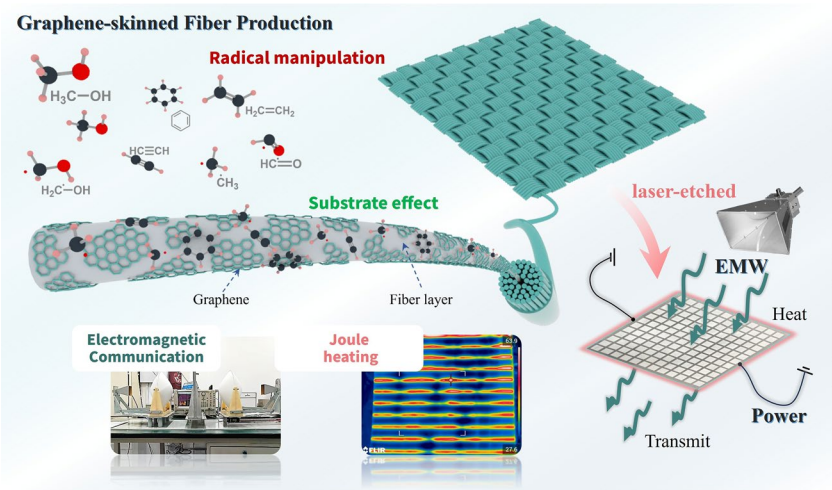

KEYWORDS Graphene; Fiber; Radical manipulation; Electromagnetic wave; Joule heating

✉ Fang Ye, yefang511@nwpu.edu.cn; Xiaomeng Fan, fanxiaomeng@nwpu.edu.cn; Qiang Song, songqiang511@nwpu.edu.cn
[1] Science and Technology On Thermostructural Composite Materials Laboratory, Northwestern Polytechnical University, Xi'an 710072, People's Republic of China

Published online: 02 March 2026

1 Introduction

Owing to their exceptional intrinsic mechanical strength, fibrous materials are widely employed in fabricating fiber-reinforced composites (FRCs) with metallic, ceramic, or polymeric matrices. The rapid advancement of electronic information technologies and living standards has generated new demands for high load-capacity FRCs with multifunctional capabilities, including Joule heating, electromagnetic wave (EMW) communication, absorption, shielding, and deicing [1–3]. Conventional fibers (e.g., glass, carbon, aramid) are typically categorized as either high-resistance or high-conductivity materials, rendering them inadequate for such multifunctional requirements. Consequently, fiber modification has become essential to address contemporary application needs. Graphene (Gr), a two-dimensional atomic crystal, exhibits numerous superior physical properties [4–6]. Thus, the electrical properties can be improved by producing graphene-modified fibers (termed Gr-skinned fiber) [7, 8]. Nevertheless, insufficient electrical tunability of current Gr-skinned fiber restricts their applicability across diverse scenarios.

Electrical property tuning refers to the strategic modulation of electrical conductivity within a target range through process control or other methodologies. Liu et al. employed a wet-chemistry assembly process to modulate the electrical properties of aramid fibers by adsorbing varying amounts of Gr and carbon nanotubes onto their surface. However, as their approach did not involve engineering the Gr microstructure, it had a limited ability to achieve precise control over the electrical characteristics [9]. Park et al. utilized dopants including melamine, red phosphorus, and sulfur powder to synthesize N-doped, P-doped, and S-doped reduced graphene oxide (rGO) fiber with elemental concentrations of 6.52, 4.43, and 2.06 at%, respectively. The P-doped and S-doped rGO fiber exhibited conductivity enhancements of 33% and 28% over pristine rGO fiber, while N-doped rGO fiber achieved the highest conductivity of 1.11×10^4 S m^{-1} [10]. Complementarily, Witjaksono et al. demonstrated N-doped Gr with a maximum nitrogen concentration of ~ 5.51 at%, confirming monotonic conductivity improvement with increasing doping levels [11]. Spectroscopic analysis revealed a pyrrolic-N-dominated configuration in N-rGO samples, which facilitates π-bond reinforcement in carbon lattices by suppressing Stone–Wales defects and establishing electron percolation pathways. This mechanism effectively eliminates conduction gaps and enhances n-type conductivity. Nevertheless, doping strategies face inherent challenges in precise control and fine-tunable limitations due to dopant inhomogeneity and stability issues.

During chemical vapor deposition (CVD), high-temperature pyrolysis of carbon precursors generates alkane-derived molecular fragments, which serve as critical gaseous intermediates for subsequent Gr deposition [8, 12]. Modulating these radical reactions represents a primary pathway for controlling intermediate concentrations and, consequently, tailoring Gr microstructure. C_1 (CH_3·), C_2 (C_2H_2), and C_6 (C_6H_6) species constitute key deposition precursors. C_1/C_2 fragments promote isotropic or low-texture pyrolytic carbon formation while providing high-reactivity carbon sources to sustain deposition rates. C_6 aromatics facilitate stacking into highly ordered lamellar structures due to their spatial configuration [13–15]. Strategic balancing of these precursor ratios enables controlled transitions from isotropic to highly textured Gr architectures. When utilizing oxygen-containing precursors like methanol (CH_3OH), pyrolysis co-generates H_2O and CO_2 byproducts that induce edge etching effects on carbon clusters [16, 17]. Precursor concentration modulation thus provides a viable route for Gr manipulation crystallographic orientation and electrical properties.

In this work, Gr was synthesized on SiO_2 fiber surfaces via low-pressure chemical vapor deposition (LPCVD) using CH_3OH as the carbon precursor. Through elementary reaction modulation, controlled ratios of C_1, C_2, and C_6 species were achieved. Under lower temperatures, incomplete CH_3OH pyrolysis yielded C_1-dominant precursors, promoting multi-site nucleation on rough fiber surfaces. This inhibited sufficient crystallite growth, resulting in low-texture Gr with reduced electrical conductivity. Conversely, higher temperatures facilitated complete pyrolysis, enriching C_6 species that suppressed nucleation density and enabled large-crystallite, high-texture Gr with enhanced conductivity. H_2O and CO_2 byproducts induced edge etching, preferentially facilitating multilayer Gr growth. As deposition progressed, substrate effects diminished significantly, producing stratified Gr layers with distinct structural properties between basal and surface regions. Consequently, synergistic precursor control and substrate effect modulation enabled fine-tuning of sheet resistance within 26–150 Ω sq^{-1}. To address multifunctional electro-thermal requirements,

https://doi.org/10.1007/s40820-026-02117-8

FSS-patterned Gr-skinned SiO_2 fabric was fabricated via galvanometer laser scanning. The architecture exhibited a remarkable electro-thermal synergetic performance, with a surface temperature of 80 °C being attained when connected to an external 105 V voltage. Concurrently, 70% EMW transmittance was maintained across a frequency range of 14.7–18 GHz. This work establishes a methodology spanning atomic-scale structural control to macroscale functional design, highlighting Gr-skinned fiber as promising candidate materials for multifunctional composite systems.

2 Experimental Section

2.1 Preparation of Gr-Skinned SiO_2 Fabric

Gr was deposited on SiO_2 fiber fabric using CH_3OH as the carbon precursor to synthesize Gr-skinned fabric. The substrate was positioned within a custom-built deposition furnace, followed by vacuum evacuation and temperature ramping. Upon reaching the target deposition temperature (1000–1200 °C), methanol vapor was introduced under controlled pressure conditions (6–8 kPa). Following the prescribed deposition time (0.5–3 h), the gas supply was terminated and systematic cooling was initiated. All samples are designated in the nomenclature *x*–*y*, where *x* denotes the deposition temperature, and *y* represents the deposition time.

2.2 Preparation of ET-Gr-Skinned SiO_2 Fabric

The Gr-skinned fabric was positioned on a laser scanning stage, where the pre-designed etching pattern was imported into the control system to initiate laser ablation. Processing parameters were configured as follows: laser power = 40 W, pulse frequency = 100 Hz, scan velocity = 1000 mm s^{-1}, line width = 0.1 mm, and line distance = 0.1 mm.

2.3 Electromagnetic Parameters Testing

Reflectance (R), transmittance (T), and absorptivity (A) were measured via the waveguide method, employing a vector network analyzer (MS4644A, Anritsu, Japan) within the 8.2–12.4 GHz. Specimen size of Gr-skinned fabric is $22.86 \times 10.16 \times 0.25$ mm^3. Furthermore, large-scale samples of SiO_2 fabric, Gr-skinned fabric, and etched (ET) Gr-skinned fabric were characterized using the free-space method across the 8–18 GHz frequency range, and the size of specimens is $180 \times 180 \times 0.25$ mm^3. A comprehensive evaluation of the electromagnetic and Joule heating properties of an integrated sandwich structure composed of an ET Gr-skinned fabric sandwiched between two acrylic plates was conducted. The structure consists of a 3-mm thick acrylic top layer, a fabric interlayer, and a 3-mm thick acrylic bottom layer. After fabricating the composite sandwich structure, it was connected to a power supply and placed in a free-space test setup, allowing for the simultaneous measurement of its electromagnetic performance during the Joule heating process.

2.4 Characterization

The morphology and microstructure of the samples were characterized by scanning electron microscope (SEM, Helios G4, FEI, USA), transmission electron microscope (TEM, Themis Z, FEI, USA), X-ray photoelectron spectroscopy (XPS, Axis Supra, Kratos, UK), and Raman spectroscopy (InVia, Renishaw, excited by a 532 nm He–Ne laser with a laser spot size of 1 μm^2). To facilitate TEM observation of Gr structures, the Gr-skinned SiO_2 fibers were immersed in 0.1 mol L^{-1} HF for 4 h, followed by ethanol washing to obtain pure Gr samples. The carbon content of the samples was quantified using a carbon–sulfur analyzer (LECO, CS844, USA). For the measurement of sheet resistance (R_s), a four-probe test was conducted using an M-3 Mini type four-probe tester (Suzhou Ijingge Electronic Co., Ltd., China) with a probe spacing of 2 mm, and measurements were performed at 10 mm intervals across the sample surface.

All calculations were carried out for the material in the framework of density functional theory (DFT) using the Vienna Ab initio Simulation Package (VASP 6.3.0). The generalized gradient approximation (GGA) of the Perdew–Burke–Ernzerhof (PBE) function was used to describe the exchange–correlation energy. The projected augmented wave (PAW) method and pseudopotentials were used to describe the interactions between valence electrons and ions. To ensure the efficiency of the computational results and parallel computing. A $4 \times 4 \times 1$ k-point grid under Monkhorst–Pack is used in the optimization process, and 500 eV truncation energy is set. The lattice parameters and ionic

positions of all crystals were fully relaxed, and the convergence criteria for the total energy of all relaxed atoms and the final force were 10^{-5} and 0.05 eV $Å^{-1}$, respectively. The SiO_2 fiber surface was assumed to have an α-SiO_2 (001) structure. It should be noted that our calculations employ an idealized flat SiO_2 (001) surface to reveal the fundamental influence of its polarized chemical nature on precursor behavior. The roughness and curvature of actual SiO_2 fibers, by introducing microscopic defects, would further increase the effective diffusion barriers and provide additional nucleation sites. Consequently, the restrictive effect of the SiO_2 substrate in real environments is likely more pronounced than our model predicts.

3 Results and Discussion

3.1 Radical Manipulation

The gas-phase reaction process provides the essential material foundation for solid-phase deposition and represents the dominant reaction pathway in gas pyrolysis (Fig. 1a). To accurately describe methane gas-phase pyrolysis within CVD and quantify concentrations of pyrolysis products, elucidating the underlying gas-phase reaction mechanism of methane pyrolysis is imperative. CVD processes typically employ tubular reactors, commonly approximated as plug-flow reactors [18]. CH_3OH gas is introduced into such a plug-flow reactor to analyze its gas-phase pyrolysis behavior. The reaction zone consists of a straight cylindrical tube devoid of internal structures, thus resulting in a low specific surface area. Consequently, the deposition rate of solid pyrolytic carbon approaches zero, rendering it negligible. CH_3OH is vaporized via a water bath and fed into the reactor inlet, where reactions proceed at 1273 K under a pressure of 8 kPa. Within the reaction zone (10 cm of length, 5 cm of diameter, Fig. 1b), gases react during a defined residence time before products exit through the outlet. Figure 1c illustrates residence times at distinct axial positions, indicating a progressive increase toward the reactor outlet. Figure 1d depicts species mole fractions, revealing that CO_2 and H_2O, byproducts of CH_3OH significantly exceed the concentrations of hydrocarbons such as $CH_3\cdot$, C_2H_2, and C_6H_6.

In the CVD of carbon-based materials, Gr deposition reactions are primarily classified into three categories (C_1, C_2, and C_6) based on gaseous carbon source species capable of deposition. Prior mechanistic studies indicate that methyl radicals ($CH_3\cdot$) serve as the dominant carbon source for Gr deposition. Acetylene (C_2H_2) deposits Gr via surface addition reactions, while increased concentrations of C_6 species (e.g., benzene rings) enhance the structural ordering of the deposited pyrolytic carbon [19–21]. CO_2 enables selective etching of small crystallites, thereby reducing grain boundary density and enhancing Gr texture [22]. Qi et al. demonstrated that H_2O etches edges of upper-layer Gr while promoting basal-layer growth, facilitating uniform multilayer Gr formation [23]. Consequently, the relative concentrations of three carbon radicals and two byproducts critically govern Gr's crystallographic structure and defect architecture.

Sensitivity analysis was employed to evaluate the influence of elementary reactions on the concentrations of major gaseous species during pyrolysis [24, 25]. The sensitivity coefficient for a given species is defined as the partial derivative of its mole fraction with respect to the kinetic parameters of the reaction. A positive sensitivity value indicates that the elementary reaction promotes the formation of the species, whereas a negative value signifies that it facilitates consumption. The absolute magnitude of the sensitivity reflects the strength of this promoting effect. Figure 1e displays the sensitivity coefficients affecting methane (CH_4) concentration. The forward reaction $OH\cdot + CH_3\cdot\ (+M) \rightarrow CH_3OH\ (+M)$ exhibits the highest positive sensitivity, indicating its dominant role in enhancing CH_4 formation. Conversely, the reaction $CH_3OH + H\cdot \rightarrow CH_2OH\cdot + H_2$ demonstrates negative sensitivity, confirming its inhibitory effect on CH_4 generation. Figure S1 shows the sensitivity coefficients of the main reactions affecting C_2H_2 and C_6H_6.

To elucidate species transformation pathways during CH_3OH gas-phase pyrolysis in CVD, dominant reaction networks were analyzed at a residence time of 0.3 s. Initial CH_3OH consumption proceeds through two primary pathways: (1) thermal decomposition ($CH_3OH \rightarrow CH_2OH\cdot + H\cdot$) and (2) radical-mediated reaction ($CH_4 + CH_3\cdot \rightarrow C_2H_5\cdot + H_2$). The hydroxymethyl radical ($CH_2OH\cdot$) subsequently reacts with formaldehyde (CH_2O) to form formyl radical ($HCO\cdot$) and CH_3OH. As revealed in Fig. 1f, $HCO\cdot$ serves as the fundamental precursor for C_2 and C_6 species generation. However, $\cdot HCO$ exhibits high reactivity and predominantly decomposes to $H\cdot$ and CO ($HCO\cdot \rightarrow H\cdot + CO$), with less than 1% participating in ethyl radical formation via reaction with C_2H_4. This low $HCO\cdot$ to

https://doi.org/10.1007/s40820-026-02117-8

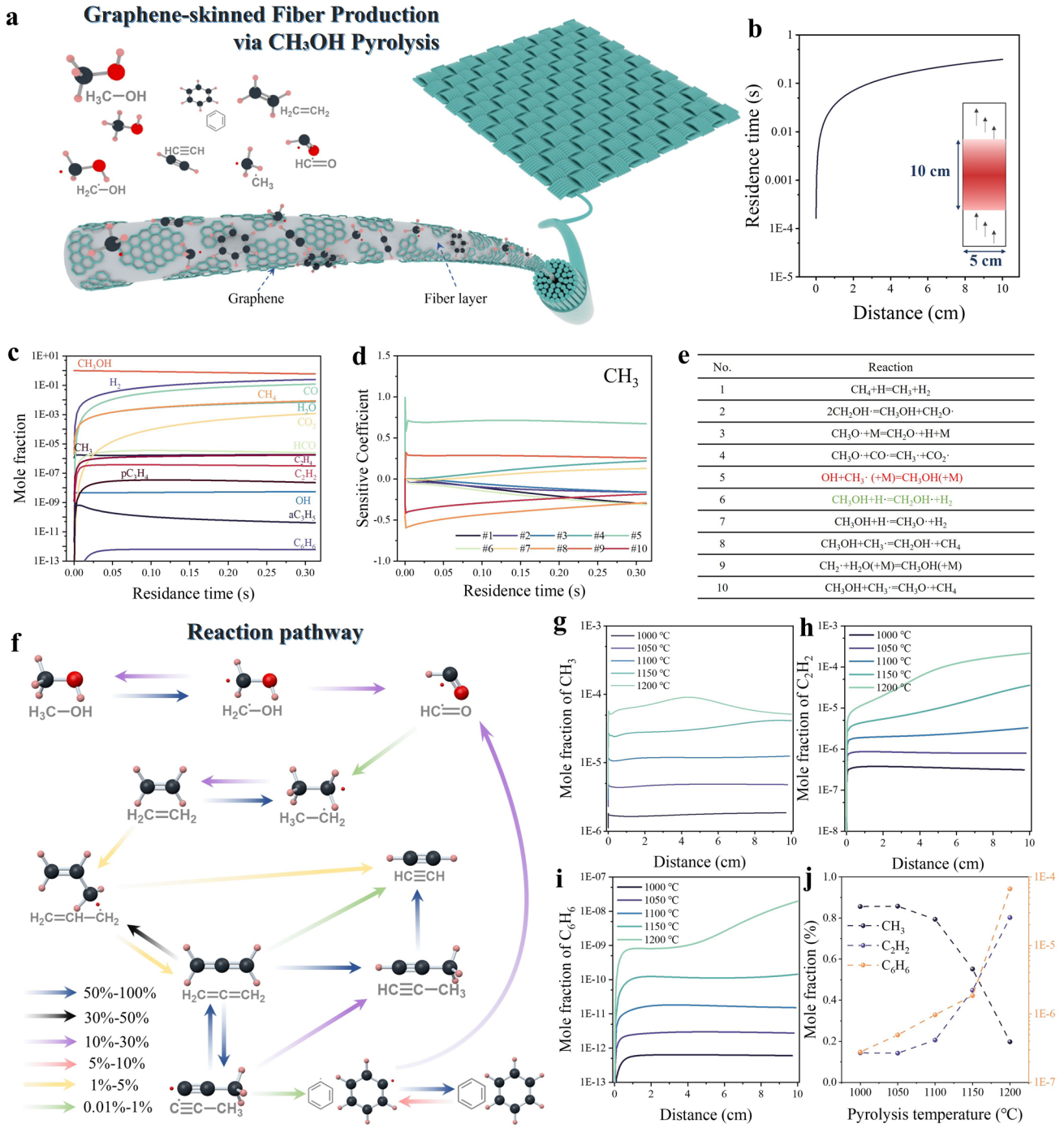

Fig. 1 **a** Schematic diagram of CH_3OH high-temperature pyrolysis. **b** Relaxation time at different positions in the reactor (inset: reactor model), **c** variation of different gas molar fractions with residence time, **d** sensitivity analysis of CH_3·, **e** the top 10 elementary reactions affecting the sensitivity of the CH_3·, **f** reaction pathway at a relaxation time of 0.15 s, **g** molar fraction of CH_3·, **h** molar fraction of C_2H_2, **i** molar fraction of C_6H_6 at different temperatures, **j** ratio of the three gases (CH_3·, C_2H_2, and C_6H_6)

C_2H_5· conversion efficiency directly accounts for the minimal C_6H_6 mole fraction (~ 10^{-12}).

To modulate key carbon source concentrations, CH_3OH pyrolysis products were computationally evaluated across varying temperatures. Figures 1g–i and S2 demonstrate that

elevated temperatures reduce residence time while concurrently increasing mole fractions of CH_3·, C_2H_2, and C_6H_6. The ratio of C_2H_2 and C_6H_6 in the three gases gradually increases, while the ratio of CH_3· decreases (Fig. 1j). Higher concentrations of gaseous products promote deposition reactions of C_2 and C_6 species, thus expanding pyrolytic carbon deposition pathways. These enable structural evolution toward either perfect hexagonal rings through single-precursor deposition or paired pentagon-heptagon topological defects via combined precursors. Consequently, deposition rates increase significantly, facilitating the growth of highly oriented Gr-like nanostructures [26–28]. The offline gas chromatographic analysis conducted under actual CVD conditions is presented in Fig. S3. Although quantitative deviations are observed due to sampling limitations and model idealization, the experimental data are shown to be in high qualitative agreement with the chemical kinetic simulations. An increase in deposition temperature is demonstrated to enhance the content of CH_4 and C_2H_2. Consequently, the mechanism, whereby the Gr microstructure is modified through the regulation of key radical distribution by temperature, is robustly validated.

3.2 Microstructure of Graphene

Building on the CH_3OH pyrolysis calculations, temperature significantly influences the types and concentrations of radical species generated during pyrolysis, thereby governing the structural characteristics of deposited Gr. Consequently, we experimentally investigated the impact of deposition temperature on Gr structure. Using CH_3OH as the carbon source with a fixed deposition duration of 1 h, Gr-skinned SiO_2 fiber were synthesized at five discrete deposition temperatures (1000, 1050, 1100, 1150, and 1200 °C), designated as 1000-1, 1050-1, 1100-1, 1150-1, and 1200-1, respectively. Figures 2a_1–e_1 and a_2–e_2) present SEM images of the five specimens, revealing incomplete Gr coverage on fiber surfaces for 1000–1 and 1050-1, indicating insufficient surface deposition under lower temperatures. Uniform Gr deposition was achieved at temperatures exceeding 1050 °C. Carbon content (mass fraction) quantified via carbon–sulfur analysis demonstrates minimal fluctuations across triplicate measurements, with values increasing proportionally to deposition temperature (Fig. S4). The average carbon contents for the five specimens were 0.048%, 0.054%, 0.065%, 0.080%, and 0.097%, respectively. Consistent with CH_3OH pyrolysis simulations, deposition uniformity correlates directly with deposition kinetics. Elevated temperatures enhance CH_3OH decomposition efficiency, yielding higher deposition rates, which aligns precisely with computational pyrolysis results.

Microstructural analysis of Gr was performed via TEM, as shown in Fig. 2a_3–e_3. No significant variation in Gr thickness was observed across temperatures, with all specimens maintaining approximately 3 layers. However, distinct textural evolution emerged with increasing temperature. Selected-area electron diffraction (SAED) patterns confirm polycrystalline structures for all specimens (Fig. 2a_4–e_4). The 1050-1 sample displays sparser diffraction spots within the rings, indicating larger crystalline domains and fewer grain boundaries (edge defects). In contrast, 1100-1 exhibits substantially increased spot density with bright, continuous rings, signifying heightened boundary defects. As temperature increases further, reduced spot density in SAED patterns demonstrates the population of differently oriented crystals diminished.

XPS analysis of the C 1*s* bonding states in Gr was performed (Fig. S5). Peak deconvolution reveals four distinct bonding configurations: C–C bonds (284.8 eV), defect-associated peaks (primarily C–H, 285.4 eV), C–O bonds (286.5 eV), and π-π transitions (291.0 eV) [29–31]. The C–C bonds correspond to sp^2 hybridization, serving as an indicator of graphitic ordering. Defect peaks signify edge defects, while C–O bonds reflect oxygen-induced sp^3 hybridization. Quantitative analysis across deposition temperatures (Fig. S5) demonstrates a non-monotonic temperature dependence: C–C content initially increases, declines at intermediate temperatures, and subsequently rises again, peaking at 1050 °C. Conversely, defect concentration follows an inverse trend, reaching its maximum at 1100 °C. These XPS results corroborate TEM observations, collectively indicating altered structural characteristics in Gr synthesized above 1050 °C.

Raman spectroscopy, being exquisitely sensitive to carbon structural features, was employed for further microstructural characterization of Gr, as presented in Figs. 3a and S6. The spectra exhibit characteristic D, G, and 2D peaks, confirming the Gr structure. The D band at 1350 cm^{-1} arises from lattice defects, predominantly armchair-edge defects. The G band at ~ 1580 cm^{-1} corresponds to in-plane vibrational modes of sp^2-hybridized carbon atoms. Crucially, both the position and full width at half maximum (FWHM) of the

https://doi.org/10.1007/s40820-026-02117-8

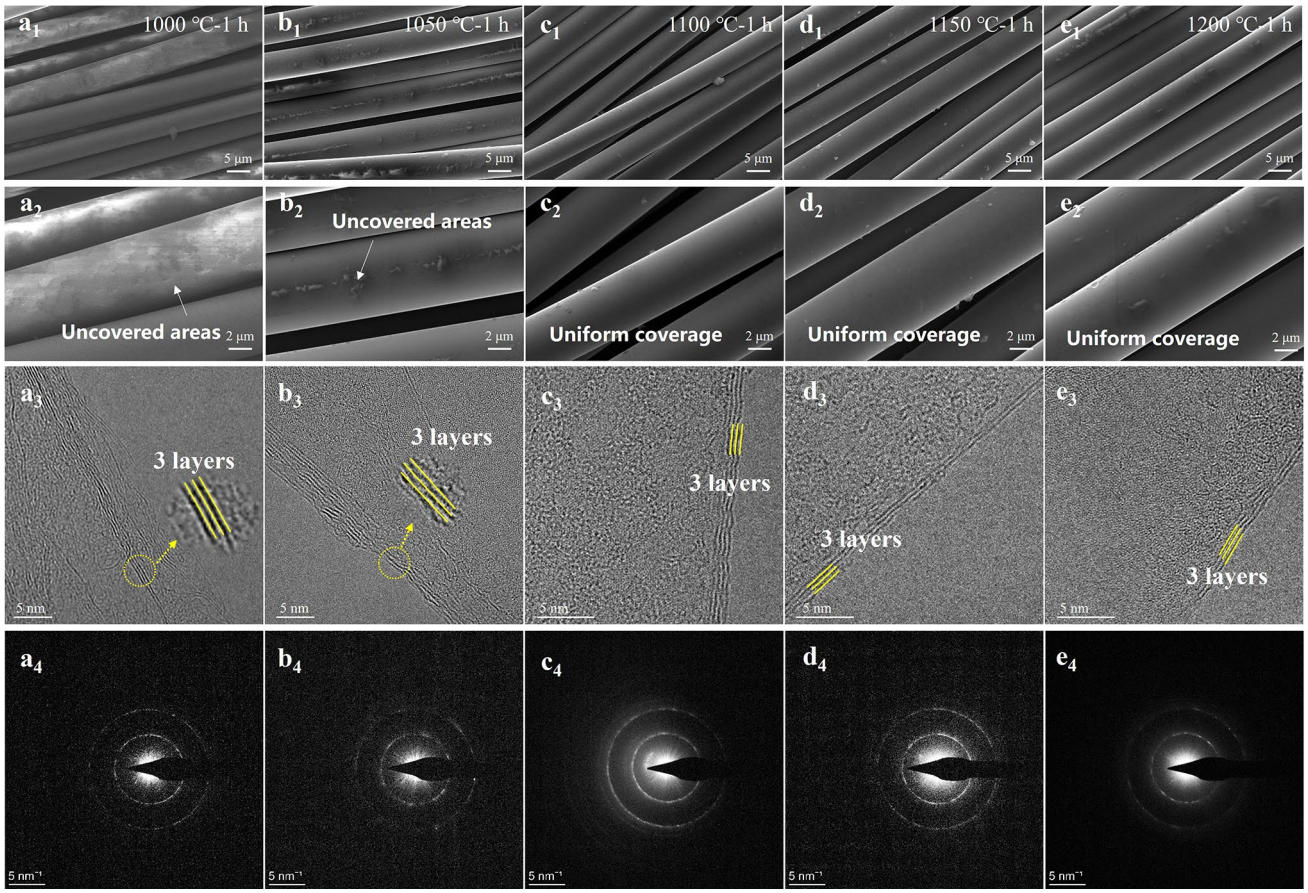

Fig. 2 Micromorphology of Gr-skinned SiO_2 fiber: $\mathbf{a_1}$-$\mathbf{a_2}$ 1000 °C-1 h, $\mathbf{b_1}$-$\mathbf{b_2}$ 1050 °C-1 h, $\mathbf{c_1}$-$\mathbf{c_2}$ 1100 °C-1 h, $\mathbf{d_1}$-$\mathbf{d_2}$ 1150 °C-1 h, $\mathbf{e_1}$-$\mathbf{e_2}$ 1200 °C-1 h. Microstructure of Gr $\mathbf{a_3}$ 1000 °C-1 h, $\mathbf{b_3}$ 1050 °C-1 h, $\mathbf{c_3}$ 1100 °C-1 h, $\mathbf{d_3}$ 1150 °C-1 h, $\mathbf{e_3}$ 1200 °C-1 h. Selective electron diffraction of Gr: $\mathbf{a_4}$ 1000 °C-1 h, $\mathbf{b_4}$ 1050 °C-1 h, $\mathbf{c_4}$ 1100 °C-1 h, $\mathbf{d_4}$ 1150 °C-1 h, $\mathbf{e_4}$ 1200 °C-1 h

G band serve as metrics for structural disorder manifested through distorted hexagonal rings and chains: Increased disorder typically leads to a blue shift while broadening the FWHM. The 2D band at ~ 2700 cm^{-1} indicates high-quality Gr and exhibits layer-dependent intensity, diminishing with increasing layer count. Additionally, the D′ band at ~ 1625 cm^{-1} is diagnostic of zigzag-edge defects [32–34]. Due to its spectral proximity to the G band, deconvolution was essential to resolve overlapping features (Fig. 3b–f). While the 1000-1 specimen shows distinct D, G, and D′ bands, the 1050-1 sample displays D′ band disappearance and reduced D-band intensity. Notably, above 1050 °C, the G-band region resolves into two overlapping peaks. A low-intensity peak at lower wavenumbers (Peak 2) and a high-intensity peak at higher wavenumbers (Peak 1).

According to Cançado et al. [35], when probing bilayer carbon materials with distinct structural features, laser-intensity-dependent G-band shifts occur due to thermal effects. Guided by this finding, Raman analysis was performed on Gr at laser intensities of 5%, 10%, 50%, and 100% (Fig. 3g). Increasing laser intensity induces progressive red shifting of Peak 1, while Peak 2 remains spectrally invariant (Fig. 3h–k). This divergence likely originates from differential thermal dissipation pathways: Surface Gr layers experience efficient heat dissipation, whereas underlying Gr undergoes thermal expansion due to constrained heat transfer through the thermally insulating fiber substrate. Consequently, Peak 1 and Peak 2 likely originate from subsurface and surface Gr layers, respectively. Furthermore, the relative intensities of G1 and G2 bands correlate with their growth chronology: The subsurface Gr layer nucleates preferentially, achieving higher deposition yield that manifests as enhanced G1 band intensity. Surface Gr initiates nucleation only after uniform subsurface growth, resulting

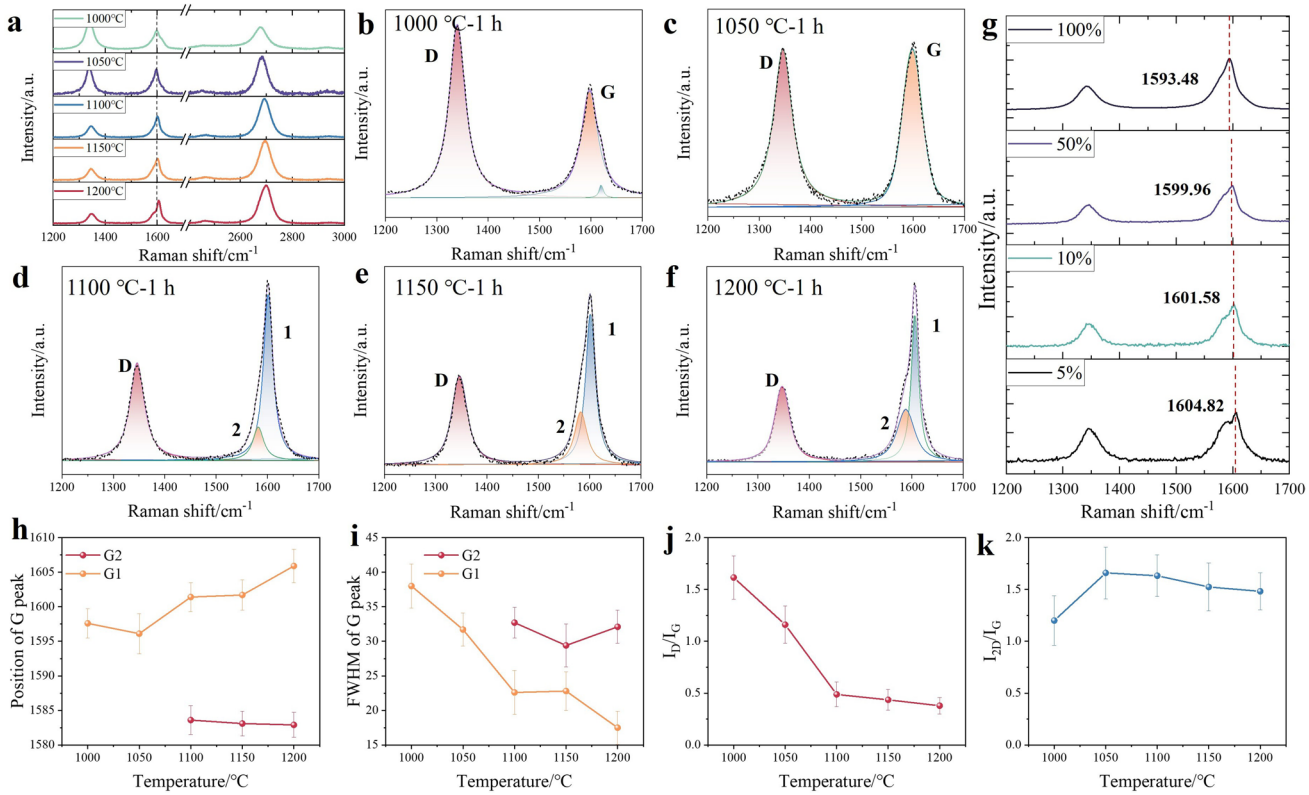

Fig. 3 Raman spectra of Gr at different deposition temperatures: **a** Broadband spectrum, fine spectrum of **b** 1000 °C-1 h, **c** 1050 °C-1 h, **d** 1100 °C-1 h, **e** 1150 °C-1 h, **f** 1200 °C-1 h. **g** Raman spectra of Gr at different laser intensities. **h** G peak position, **i** FWHM of G peak, **j** I_D/I_G, **k** I_{2D}/I_G

in lower areal density due to shorter deposition time and thus diminished G2 intensity. Further analysis in conjunction with carbon content test results, specimens 1000-1 and 1050-1 exhibit minimal deposition yields and slow growth kinetics, explaining the absence of G2-type Gr. Conversely, accelerated deposition rates in 1100-1, 1150-1, and 1200-1 promote progressive formation of surface G2-type Gr with increasing temperature.

3.3 Substrate Effect

To further validate the bilayer Gr architecture, deposition time was extended. Figures 4a1–e1 and a2–e2 present SEM images of specimens synthesized at 1050 and 1200 °C across different deposition times. At 1050 °C with inherently slower deposition rate, complete Gr coverage on SiO_2 fiber requires deposition time more than 2 h (Fig. 4a_2). At 1200 °C, discontinuous Gr coverage persists during initial deposition less than 1 h. Prolonged deposition achieves uniform surface coverage, with discernible proliferation and dimensional growth of densely packed nanosheets (multilayer island, Fig. 4e_2). The Gr content at different deposition times at 1200 °C was tested using a carbon and sulfur analyzer. The results showed that it increased with the deposition time, and the average values of carbon content of the 1200-0.5, 1200-1, 1200-2, and 1200-3 were 0.072%, 0.097%, 0.109%, and 0.132%, respectively. Corresponding TEM characterization (Fig. 4f_1–g_1) reveals layer multiplication from 3 to 10 layers with deposition time increase. Figure 4f_2–g_2 displays the superimposed in-plane projection of multi-layer graphene. The observed complexity in the carbon atom arrangement is due to the overlapping of several graphene lattices with different crystallographic orientations. SAED (Fig. 4f_3–g_3) further corroborates this stratification, showing increased spot density in diffraction patterns indicative of enhanced crystallite population with different orientations.

Raman results showed that the G2 peak appeared in the sample at 1050 °C when the deposition time reached 3 h. The deposition time was extended at 1200 °C, and the G2

 https://doi.org/10.1007/s40820-026-02117-8

peak gradually enhanced and exceeded the G1 peak. In order to provide a comprehensive explanation for the microstructure evolution of Gr with the change of deposition time, we thoroughly investigated the Raman spectral evolution presented in Fig. S7, which covers samples prepared from 1000 to 1200 °C for 1 to 3 h. As demonstrated in Fig. 4h, i, more comprehensively, in Fig. S7a, the Gr prepared at 1000 °C exhibited G2-type Gr after 3 h, which can be attributed to the low deposition rate at this temperature. The full spectral series in Fig. S7 shows that this resulted in uniform coverage of the substrate surface after 2 h. The I_D/I_G of different deposition times was calculated to be 1.62, 1.25, and 0.86, respectively. The monotonically decreasing I_D/I_G trend shown in Fig. S7 is due to the fact that the G1-type Gr is still in the growth stage before 2 h. As the growth progresses, the Gr sheet gradually grows and the edge defect content decreases. The I_{2D}/I_G of different deposition times at 1000 °C is 0.91, 0.91, and 0.82, respectively. This finding indicates that the number of Gr layers remains constant when the deposition time is less than 2 h. These data from Fig. S7 corroborate the hypothesis that G1-type Gr remains in the growth stage when the deposition time is less than 2 h, and that the presence of G2-type Gr is absent in these conditions.

As clearly illustrated by the comparative spectra in Fig. S7b, the Raman spectra of Gr prepared at 1050 °C for varying deposition times are presented. Its structural characteristics are highly similar to those of Gr prepared at 1000 °C. When the deposition temperature exceeds 1050 °C, the temporal evolution of Gr structure characteristics, fully captured in Fig. S7c-e, manifests a distinct mode. It is evident from the spectral sequence that the nucleation of G2-type Gr has already begun to exist in 1100-1, 1150-1, and 1200-1. Consequently, the relative intensity of G1 peak gradually decreases, while the relative intensity of G2 peak gradually increases with the extension of deposition time. Furthermore, the I_D/I_G increases with deposition time, which may be attributed to the ongoing nucleation of G2 type Gr, resulting in a substantial number of edge defects being contributed by small-sized carbon clusters. The calculated I_{2D}/I_G ratio decreases with an increase in deposition time, indicating that the number of Gr layers continues to increase. However, the structural characteristics of Gr prepared at 1200 °C are slightly different from those at 1100 and 1150 °C (Fig. 4j, k). As supported in Fig. S7e, the I_D/I_G decreases with an increase in deposition time and then tends to be stable. This phenomenon can be attributed to the growth of G2-type Gr nanosheets, concomitant with a decline in nucleation rate, leading to a reduction of edge defects. Figure S8 shows the cross-section microstructure of 1200-3, exhibiting a three-layer configuration: a Pt protective top layer, an intermediate Gr layer, and an amorphous SiO_2 fiber substrate at the bottom. Notably, the Gr layer displays a distinct bilayer morphology. The sub-layer adjacent to the SiO_2 substrate contains more edge defects, exhibits lower continuity, and has a thickness of about three layers, consistent with the G1-type Gr identified by Raman analysis. In contrast, the upper sub-layer grown above it shows fewer defects and improved continuity, corresponding to the G2-type Gr characterized in the Raman results.

Based on the Raman shift difference between G1 and G2 peaks, G1 exhibits higher edge defect density and smaller crystallite size, whereas G2 features larger crystallites. This divergence primarily may originate from substrate effects. To further clarify the roles of $CH_3\cdot$, C_2H_2, and C_6H_6 in Gr nucleation and growth, the adsorption energy calculations for these three precursors on different substrate surfaces were supplemented. As shown in Fig. 4m, the adsorption energies of $CH_3\cdot$, C_2H_2, and C_6H_6 on the initial SiO_2 substrate are -1.001, -1.016, and -0.987 eV, respectively. However, on the SiO_2 substrate covered by three layers of graphene (SiO_2-Gr3, structure shown in Fig. 4l), their adsorption energies change significantly to -0.053, -0.098, and -0.802 eV, respectively. The results indicate that $CH_3\cdot$ acts as the primary driver for early stage nucleation due to its strong adsorption on SiO_2. To clarify why 3-layer Gr mark the growth transition, we constructed five surface models: pure SiO_2, and SiO_2 covered with 1 to 4-layer Gr (SiO_2-Gr1 to Gr4). The calculated $CH_3\cdot$ adsorption energies are -1.001, -0.433, -0.075, -0.053, and -0.050 eV, respectively (Fig. 4n). The adsorption energy increases with the Gr layer number, indicating progressively weaker adsorption. Notably, after three layers, the energy stabilizes, showing that three Gr layers sufficiently screen the SiO_2 substrate effect. Hence, the disappearance of the substrate effect at three layers is the key transition point, shifting the growth mechanism from $CH_3\cdot$ dominated rapid nucleation to C_6 promoted grain growth. As illustrated in Fig. 4o–q, the diffusion energy barriers of three primary monomers on two distinct substrate surfaces are demonstrated. The diffusion energy barriers of $CH_3\cdot$ on SiO_2 and Gr substrates are 0.54 and 0.43, respectively. The diffusion energy barriers of C_2H_2 on SiO_2 and Gr substrates are 1.77 and 1.55, respectively,

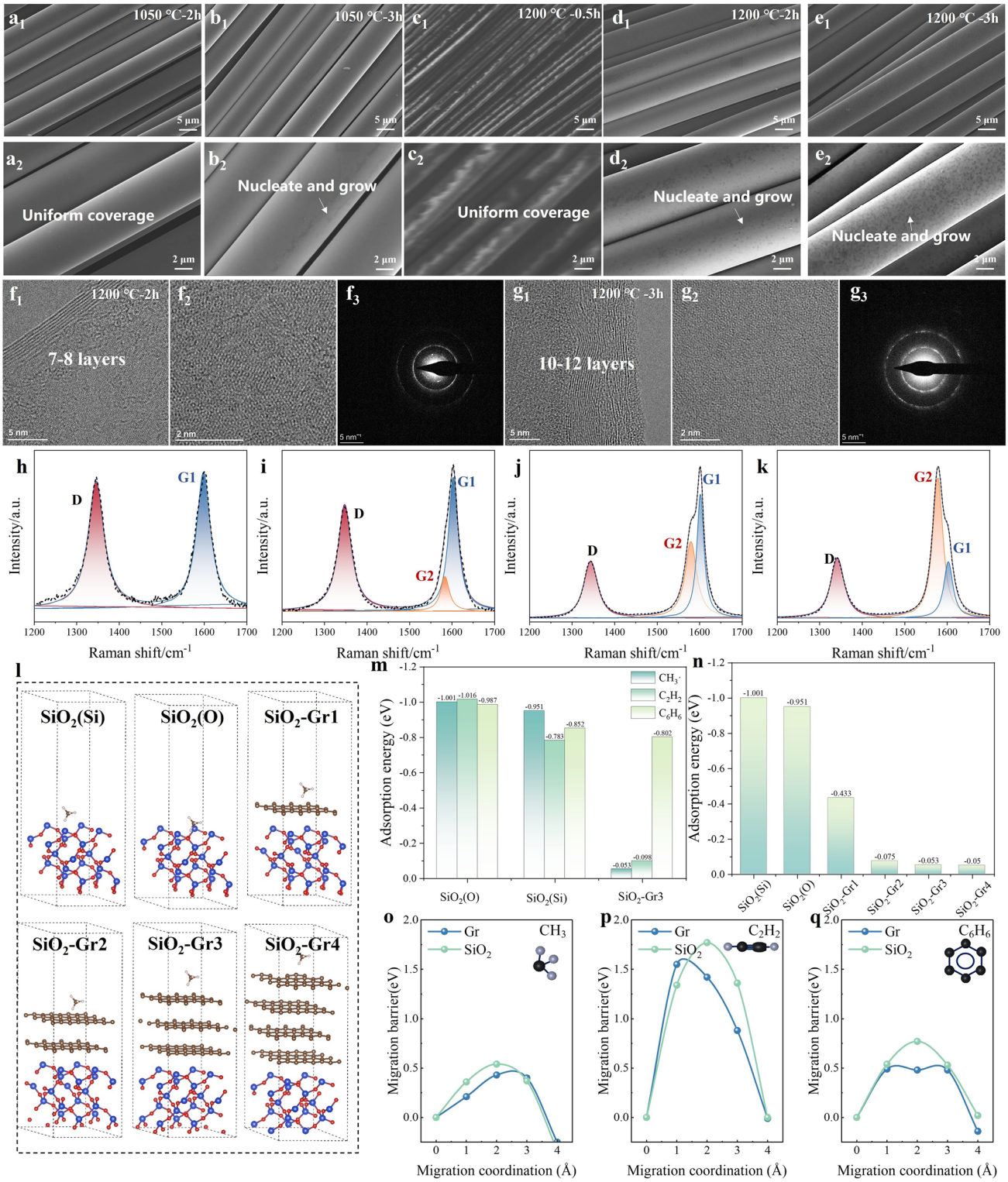

Fig. 4 Micromorphology of Gr-skinned SiO_2 fiber: **a** 1050 °C-2 h, **b** 1050 °C-3 h, **c** 1200 °C-0.5 h, **d** 1200 °C-2 h, **e** 1200 °C-3 h. Microstructure of Gr: $\mathbf{f_1}$-$\mathbf{f_2}$ 1200 °C-2 h, $\mathbf{g_1}$-$\mathbf{g_2}$ 1200 °C-3 h. Selective electron diffraction of Gr: $\mathbf{f_3}$ 1200 °C-2 h, $\mathbf{b_4}$ 1200 °C-3 h. Raman spectra of Gr at different deposition times: **h** 1050 °C-2 h, **i** 1050 °C-3 h, **j** 1200 °C-2 h, **k** 1200 °C-3 h. **l** Molecular model, **m** adsorption energy of CH_3·, C_2H_2, and C_6H_6 on the surface of SiO_2 and SiO_2-Gr3, **n** adsorption energy of CH_3· on the surface of SiO_2, SiO_2-Gr1, SiO_2-Gr2, SiO_2-Gr3 and SiO_2-Gr4. Migration energy barriers of **o** CH_3·, **p** C_2H_2, **q** C_6H_6 on two different substrates

https://doi.org/10.1007/s40820-026-02117-8

while those of C_6H_6 are 0.77 and 0.49, respectively. The results demonstrate consistently higher diffusion barriers on SiO_2 versus Gr for all precursor species. This indicates suppressed precursor mobility on SiO_2, inhibiting large crystallite formation and promoting edge defect generation. These computational findings explained that the reason of G1-type Gr contains more defects than G2-type Gr.

Different radicals precisely regulate nucleation and growth through their specific adsorption and diffusion behaviors. C_1 radicals (CH_3·): High activity, strong adsorption and difficult diffusion on the initial SiO_2 surface, inducing high-density random nucleation, resulting in small grain size and numerous grain boundary defects [19, 21]. C_2 species (C_2H_2): The weak adsorption and diffusion capabilities of the Gr surface limit its ability to promote growth [36]. C_6 species (C_6H_6): Possessing moderate adsorption energy and excellent diffusivity, capable of long-range migration and perfect epitaxial incorporation at lattice edges, effectively suppressing secondary nucleation, thereby dominating the growth of large-grained, low-defect, high-quality Gr [37]. Temperature-mediated tuning of the ratio among the three enables a switch in growth mode from "defect engineering" to "crystallization optimization".

In the initial deposition stage (Fig. 5), the pyrolysis products are predominantly linear small molecules such as CH_3· and C_2H_2, which govern the nucleation and growth of the G1-type Gr layer. These species readily adsorb onto the SiO_2 substrate, promoting rapid nucleation and initiating growth. After the out-of-plane deposition of three Gr layers, the adsorption energy of CH_3· decreases significantly, slowing further nucleation and growth. Concurrently, H_2O and CO_2 etch the edges, re-exposing active sites and accelerating lateral expansion. This stage is nucleation-dominated, yielding small Gr grains with a high density of grain-boundary defects. Once the G1-type Gr layer fully covers the substrate, the growth interface shifts to the Gr surface. At this stage, the adsorption of CH_3· and C_2H_2 on Gr weakens considerably, reducing the nucleation rate. C_6H_6, with its moderate adsorption energy and high mobility, undergoes long-range diffusion and preferentially attaches to low-energy sites such as step edges, effectively suppressing random secondary nucleation. This stage is growth-dominated, leading to larger Gr grains with fewer grain-boundary defects.

3.4 Electrical and Thermal Properties

Deposition temperature governs the types and concentrations of radical species in CH_3OH pyrolysis, while differences in deposition times fully reflect the influence of substrate effects on carbon cluster migration. Through synergistic interplay of radical regulation and substrate effects, precise microstructure engineering of Gr becomes achievable.

The electrical properties of Gr are closely related to its microstructure, whereby a higher Gr content and texture result in enhanced electrical conductivity of the composites. Therefore, the sheet resistance (R_s) of Gr-skinned fabric prepared under different deposition processes was tested (Fig. 6a). 1000-1 failed to form a continuous conductive pathway of Gr due to the slow deposition rate of Gr, thus resulting in open circuits. The lowest R_s of 1050-1, 1100-1,

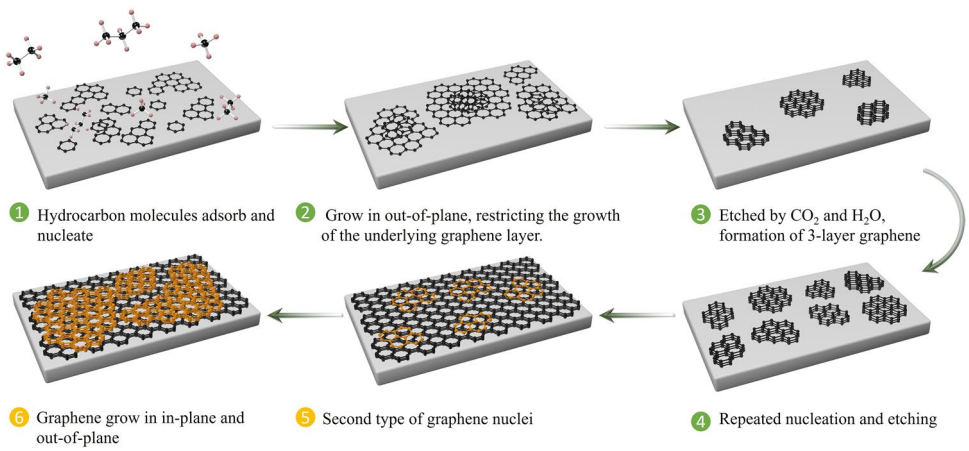

Fig. 5 Mechanisms of Gr deposition using CH_3OH as a carbon source

1150-1, and 1200-1 are 80, 66, 56, and 40 Ω sq^{-1}, respectively. It has been demonstrated that R_s decreases gradually with increasing deposition temperature. As shown in Fig. 6b, the coverage rates of samples 1000-1 and 1050-1 are 60.3% and 94.3%, respectively, while samples prepared at higher temperatures achieve 100% coverage. Notably, when the temperature exceeds 1050 °C, a marked decrease in R_s is observed, which can be attributed to the complete and uniform coverage of Gr on the substrate surface, thereby forming a continuous conductive pathway. Systematic measurements at 1000 °C over different deposition times reveal that the Rs decreases exponentially with increasing coverage, confirming that the failure to reach the percolation threshold is the primary cause of the high resistance observed in the early stage samples (Fig. S9). For 1200-3 with in-plane size of 180 × 180 mm, the lowest Rs is as low as 26 Ω sq^{-1}, and the highest Rs is only 32 Ω sq^{-1}, indicating that high deposition temperatures can achieve uniform deposition of large-size fabric under long deposition times. Existing strategies primarily focus on achieving wide R_s ranges (2-16 k, 50-2.8 k, 25-300, 11–150 Ω sq^{-1}) often via extended deposition or post-growth modifications [22, 38–40]. In contrast, our radical-manipulation CVD process emphasizes precise, fine-grained control within a practically optimal mid-range (26–150 Ω sq^{-1}). This is quantitatively superior, yielding the lowest average division value (defined as the total R_s tuning range divided by the number of discrete sample points within that range) of 8.8 Ω sq^{-1}, which demonstrates a unique capability for fine electrical property tuning essential for advanced multifunctional design.

Electromagnetic parameters of Gr-skinned SiO_2 fabric were characterized via waveguide methodology, measuring S_{11} and S_{21} to calculate reflectance (R), transmittance (T), and absorptivity (A) (Fig. 6c–e) [41, 42]. The EMW absorption in Gr originates from the synergistic effect of conductive loss and defect-induced dipole polarization loss. The overall performance is governed by the combined influence of electrical conductivity, defect density, and the resulting impedance matching. R progressively increases with deposition temperature, exceeding 60% above 1100 °C. T exhibits inverse correlation, undergoing rapid decline beyond 1000 °C. Absorptivity demonstrates a non-monotonic profile, showing strongest EMW attenuation in 1100-1. Samples with high conductivity (1150-1, 1200-1) exhibit strong conduction loss, but their severe impedance mismatch with free space leads to high R, thereby limiting A. Conversely, samples with low conductivity (1000-1, 1050-1) show good impedance matching but possess insufficient intrinsic loss capability. The unique sample 1100-1 achieves an optimal balance: Its moderate conductivity improves impedance matching, allowing more EMWs to penetrate, while its higher defect density provides significant dipole polarization loss. Consequently, this sample attains the highest absorption performance by optimizing the synergy among conduction loss, polarization loss, and impedance matching.

R, T, and A describe "how the energy is distributed" at the material interface, while shielding effectiveness (specifically, absorption shielding effectiveness here) describes "how much the energy is attenuated" as the EMW propagates through the material. These two parameters characterize the material's electromagnetic interaction performance from different dimensions. Total shielding effectiveness (SE_T) increases proportionally with temperature, comprising reflective (SE_R) and absorptive (SE_A) components representing the ratios of reflected-to-incident waves and absorbed-to-transmitted waves, respectively (Fig. S10) [43, 44]. It can be observed that the magnitude of SE_R and SE_A (Fig. S10b, c) is positively correlated with the electrical conductivity of the materials. This indicates that, disregarding the absolute value of the absorption coefficient (which is influenced by impedance matching), Gr-skinned fabrics with higher conductivity possess a stronger intrinsic capability to attenuate electromagnetic waves. This observation aligns with the generally accepted electromagnetic wave loss mechanism for conductive wave-absorbing materials, where conduction loss plays a dominant role. More importantly, dominant SE_A over SE_R reveals absorption-driven shielding, wherein incident waves are primarily dissipated through conductive pathways in Gr networks and dipole polarization at defect sites.

To evaluate the Joule heating performance of Gr-skinned fabrics, a simplified heater was fabricated. Copper foil electrodes were attached to fabric terminals and connected to a DC power supply, with temperature distribution monitored in real-time via infrared thermography. For 100 × 100 mm^2 fabrics, infrared image shows the temperature distribution of the Gr-skinned fabric under bending at thermal equilibrium (Fig. 6f). Figure 6g presents temperature–time curves across deposition temperatures. 1000-1 and 1050-1 exhibited negligible heating at 30 V due to high R_s. As shown in Fig. 6h, the Gr-skinned fabric exhibits a favorable uniform temperature distribution across its surface upon reaching thermal

 https://doi.org/10.1007/s40820-026-02117-8

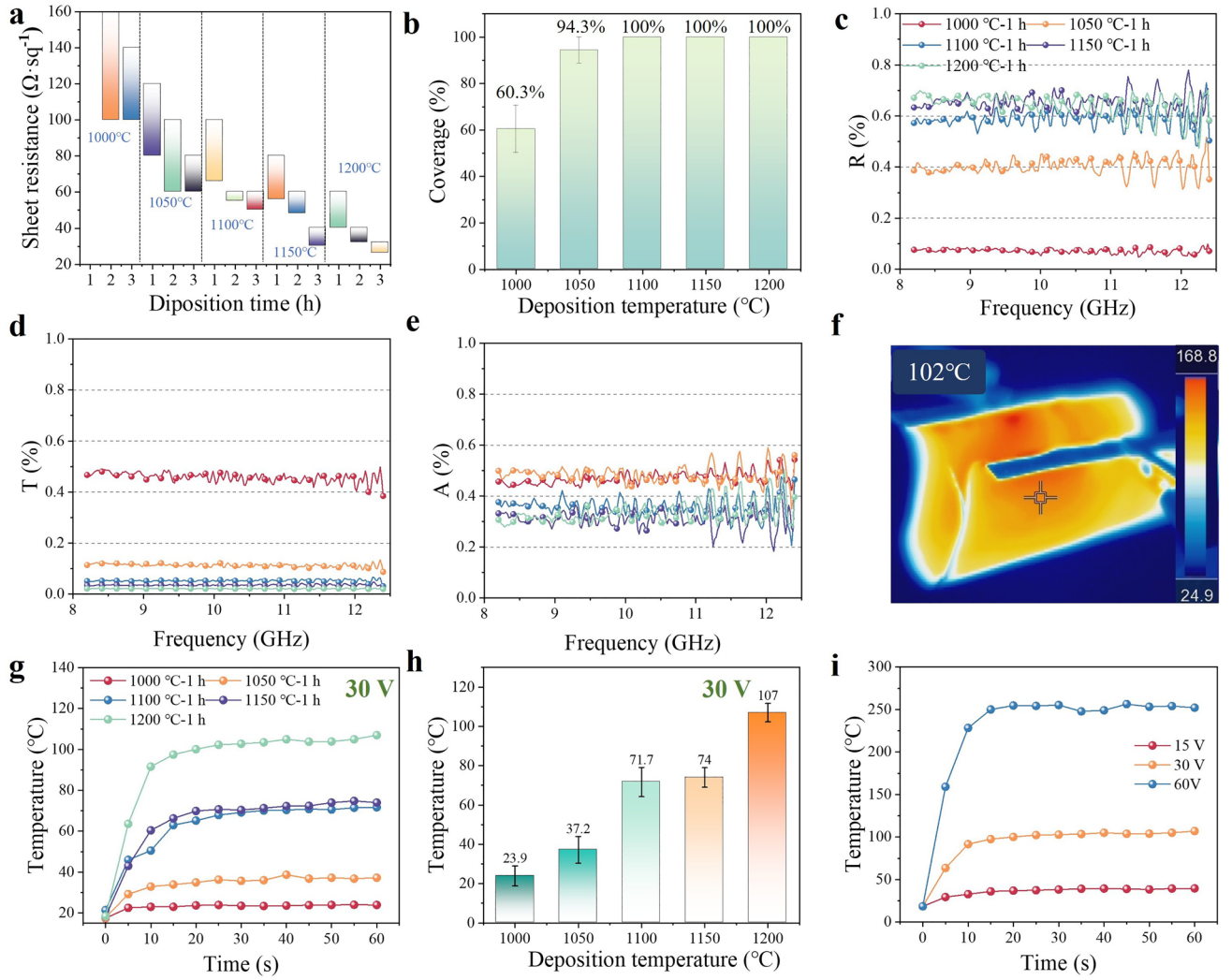

Fig. 6 **a** Sheet resistance of Gr-skinned fabric under different deposition parameters. **b** Gr coverage at different deposition temperatures. **c** Reflectance, **d** transmittance, **e** absorptance of Gr fabric at different deposition temperatures. **f** Infrared image of Gr-skinned fabric during Joule heating, **g** temperature–time curve at an applied voltage of 30 V, **h** temperature uniformity on a Gr-skinned fabric at an applied voltage of 30 V, **i** temperature–time curve of 1200 °C-1 h under different voltages

equilibrium. Elevated voltages increased heat generation following Joule law, raising radiation temperatures (Fig. 6i).

It is evident that the currently developed Gr-skinned fabric cloth lacks efficient EMW transmission capabilities. To concurrently satisfy both communication and Joule heating requirements, implementation of meta-structure for EMW modulation is necessary. Frequency selective surface (FSS) achieves modulation of EMW reflection, absorption, and transmission through periodic patterning of continuous metallic or resistive surfaces. Conventional FSS configurations are categorizable into band-pass, band-stop, high-pass, and low-pass types, as illustrated in Fig. 7a. The Gr prepared at 1200 °C possesses a superior texture and lower electrical resistance, resulting in reduced ohmic loss under an electromagnetic field. Therefore, we selected the sample of 1200-1 to evaluate its EMW transparent and electrothermal performance. T of 1200-1 was calculated for these configurations (Figs. 7b and S11). Band-pass type structures exhibit low T at low frequencies and high T at high frequencies, whereas band-stop types demonstrate inverse characteristics. Crucially, resistive high-pass and low-pass configurations diverge significantly from their metallic counterparts due to ohmic losses, which eliminate abrupt cut-off behavior. Moreover, Gr must form a continuous in-plane conductive

network to enable Joule heating functionality. Consequently, band-stop and low-pass configurations are unsuitable for this application. Reduced Gr coverage area predictably enhances T, but this simultaneously degrades Joule heating performance. Following comprehensive evaluation, the band-pass FSS configuration was selected for the integrated EMW communication and Joule heating Gr-skinned fabric. Structural parameter optimization yielded final dimensions of periodicity p of 15 mm and aperture ratio a of 0.76 [45, 46].

Based on the optimized FSS configuration, the Gr-skinned fabric was processed using laser scanning technology to create the meta-surface structured sample shown in Fig. 7c. The laser exerts both pronounced mechanical impact and thermal effects on Gr. By precisely controlling the laser power and repetition rate, selective and efficient etching of Gr-skinned fibers can be achieved without damaging the substrate, as shown in Fig. S12. The etched fiber substrate remains intact, with no signs of fracture or melting. The R, T, and A of SiO_2 fabric, Gr-skinned fabric, and etched (ET) Gr-skinned fabric were characterized via the free-space method (Fig. 7d–g). The SiO_2 fabric exhibited low R and high T, which attributable to its low permittivity and minimal thickness. In contrast, the Gr-skinned fabric showed high R (50%-60%) and A (35%-45%), with T limited to 3.3% within 8–18 GHz. After etching, the ET-Gr-skinned fabric showed significantly reduced R and enhanced T, achieving a maximum T of 77%. Its transmission characteristics exhibited frequency-selective behavior: low transmission at lower frequencies and high transmission at higher frequencies. Defining the effective transmission band (ETB) as the frequency range where transmission (T) exceeds 60%, the ET-Gr-skinned fabric exhibits an ETB of 5.66 GHz (12.34–18 GHz). Figure 7g confirms strong agreement between simulated and measured R/T values for the ET-Gr-skinned fabric. Figure 7h illustrates the Joule heating test setup for the ET-Gr-skinned fabric. Under the voltage of 60 V, infrared thermography (Fig. 7i) revealed a striped temperature distribution with localized heating up to 62.6 °C. Voltage-dependent heating tests (Fig. 7j) demonstrated monotonic temperature increase with higher voltages. The ET-Gr-skinned fabric exhibits excellent stability for wearable applications. It shows remarkable mechanical robustness, with a relative resistance change ($\Delta R/R_0$) below 0.05 under bending radii from 5 to 23 mm (Fig. 7l), due to its continuous conductive network. The fabric also demonstrates exceptional cyclic stability, maintaining a surface temperature fluctuation within ± 1 °C over 100 heating/cooling cycles (Fig. 7l), owing to the high crystallinity of the CVD-grown Gr. Furthermore, its Joule heating performance shows near immunity to humidity. The intrinsically hydrophobic surface ensures stable resistance, with only a subtle temperature decrease above 40% relative humidity attributable to enhanced evaporative cooling (Fig. 7m).

Owing to the impracticality of standalone deployment for fabric, we fabricated a sandwich structure by laminating it with acrylic sheets. To better replicate real operational conditions, a Joule heating system was integrated into the free-space measurement setup (Fig. 8a), enabling simultaneous electromagnetic characterization during thermal activation. The acrylic serves as a wave-transparent material with a relative permittivity of 2.72 - 0.02 (Fig. 8b). Infrared thermography during free-space testing (Fig. 8c) reveals a striped temperature distribution across the heated surface, while voltage-dependent surface temperatures (Fig. 8d) indicate reduced heating efficiency compared to standalone ET-processed Gr-skinned fabric. Unheated electromagnetic simulations and measurements of the sandwich structure (Fig. 8e) demonstrate excellent agreement. The sandwich configuration of the ET-Gr-skinned fabric achieved a wider ETB of 8.48 GHz (8.62–17.1 GHz), resulting from the phase modulation of electromagnetic waves by the acrylic sheets. During Joule heating, electromagnetic parameter characterization showed that R and T spectra shifted toward lower frequencies with increasing voltage, whereas A exhibited negligible variation (Fig. 8f–h). Table 1 presents the maximum T, the corresponding ETB and surface temperature of the sandwich structure under different applied voltages.

However, it must be acknowledged that the enhancement of Joule heating performance comes at the cost of a gradually narrowing ETB. As the Gr units constitute the sole loss component in this architecture, the minimal variation in A confirms the stable electrical resistance of Gr under heating at 30–120 V. To analyze the cause of the shift in the R and T curves during Joule heating, the complex permittivity of the acrylic material from 20 to 100 °C was measured, as shown in Fig. S13. The results indicate a gradual increase in the real part of the permittivity (ε'), while the imaginary part (ε'') shows relatively minor changes. Furthermore, we simulated the electromagnetic transmission characteristics of the sandwich structure with the acrylic layer at 80 °C and compared the results with those at room temperature (20 °C).

https://doi.org/10.1007/s40820-026-02117-8

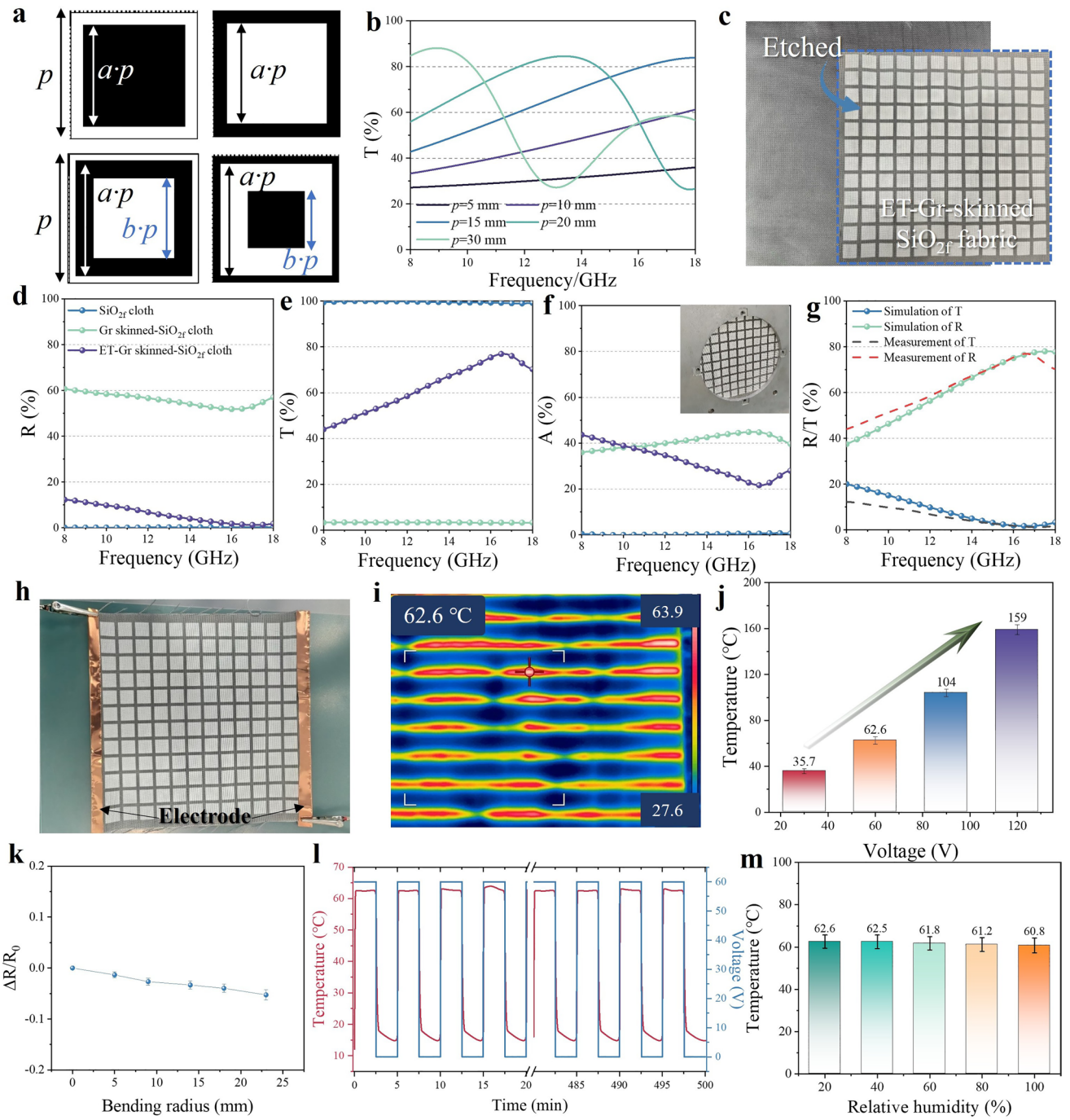

Fig. 7 **a** Schematic diagram of traditional FSS configurations, **b** transmittance of band-pass type FSS under different structural parameters. **c** Digital images of ET-Gr-skinned fabric before and after etching. **d** Reflectance, **e** transmittance, **f** absorptance of the three types of fabric (SiO_2 fabric, Gr-skinned fabric, and ET-Gr-skinned fabric), **g** simulated and measured transmittance. **h** Heating device for ET-Gr-skinned fabric, **i** infrared image of ET-Gr-skinned fabric, **j** temperature of ET-Gr-skinned fabric at different voltages, **k** electrical-resistance variation with bending radii from 5 to 23 mm, **l** temperature curves while applying a square wave from 0 to 60 V with period of 5 min for 100 cycles, **m** surface temperature at different relative humidity

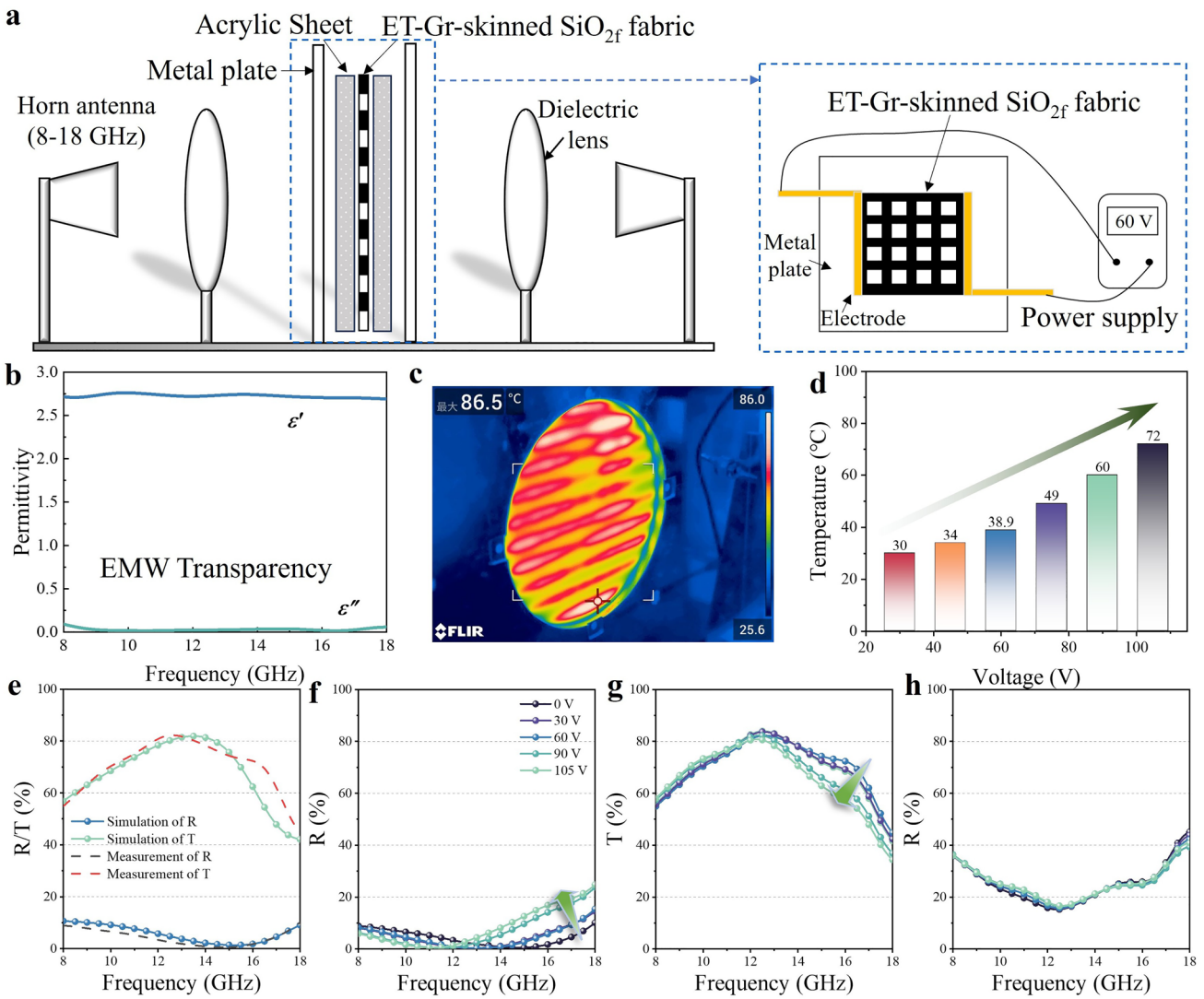

Fig. 8 **a** Free-space synchronous Joule heating test system. **b** Permittivity of acrylic. **c** Infrared image of the sandwich structure during Joule heating, **d** surface temperature of the sandwich structure at different voltages. **e** Simulated and measured transmittance values of the sandwich structure, **f** reflectance, **g** transmittance, **h** absorptance at different applied voltages

The simulations reveal subtle differences in R and T at 80 °C (Fig. S14), primarily manifesting as a shift of the R, T, and A curves towards lower frequencies in the 14–17 GHz range. These simulation results are consistent with the measured electromagnetic transmission characteristics at applied voltages up to 105 V, indicating that the temperature-dependent dielectric properties of the acrylic are the main reason for the changes in transmission performance during Joule heating. The R and T spectral shifts primarily originate from the temperature-dependent permittivity of acrylic. As the temperature increases, the permittivity changes, thereby enhancing EMW reflection (particularly at higher frequencies). At an applied voltage of 105 V, the Joule heating effect raised the surface temperature of the sandwich structure to 72 °C. Simultaneously, the structure exhibited an ETB as wide as 7.29 GHz, covering most of the X and Ku bands, and a peak transmission of 80.8% at 12.27 GHz, demonstrating a collaborative balance between broadband EMW transmission and Joule heating. These collective results verify that the Gr-skinned fabric holds significant potential for applications in the electromagnetic-thermal field.

Metal-coated fibers offer the highest conductivity and heating efficiency, with R_s as low as 0.29 mΩ sq^{-1} [47–49]. However, they are highly reflective to EMW (near-zero

 https://doi.org/10.1007/s40820-026-02117-8

Table 1 Transmittance and surface temperature of sandwich structure at different applied voltages

Voltage (V)	Surface temperature (°C)	Maximum transmittance		Effective transmission band (transmittance > 60%)		
		Position (GHz)	Value (%)	Position 1 (GHz)	Position 2 (GHz)	Value (GHz)
0	25	12.53	82.2	8.62	17.1	8.48
30	30	11.95	82.3	8.46	16.88	8.42
60	39	12.54	83.6	8.52	16.93	8.41
90	60	12.37	82.3	8.3	16.22	7.92
105	72	12.27	80.8	8.22	15.51	7.29

transmittance) and are difficult to pattern non-destructively with lasers. Carbon nanotube (CNT) fabrics provide tunable conductivity (57–245 Ω sq^{-1}) and mechanical flexibility, but their resistance typically remains in a higher range [50, 51]. Intrinsic conductive polymers like PEDOT:PSS allow some optical transmittance, yet exhibit low heating efficiency (R_s ~ 29 Ω sq^{-1} with multiple layers) and a narrow tunability range dependent on physical stacking [52]. In contrast, the methanol-CVD Gr-skinned fabric developed in this work achieves a finely tunable R_s (26–150 Ω sq^{-1}), bridging the crucial low-to-medium range for multifunctional devices. It combines rapid thermal response, high-temperature stability, and excellent laser-pattern ability. Most notably, its patterned FSS structure enables significant EMW transmittance (up to 77%) while maintaining efficient Joule heating, a balanced synergy of tunability, multifunctionality, and stability not achievable with metal, CNT, or polymer-based counterparts.

Despite the demonstrated balance between EMW transmission and Joule heating, this work has limitations. The primary constraint stems from the non-uniform temperature distribution inherent to the FSS patterning, where heat generation is localized to the conductive grids. Future efforts to overcome this challenge should focus on enhancing the in-plane thermal transport of the system. This could be achieved by integrating highly thermally conductive, wave-transparent materials (BN or Si_3N_4) as either substrates or coatings, and by further optimizing the FSS geometry to improve heating uniformity. These strategies present a promising pathway toward advanced multifunctional fabrics with fully uniform thermal management and excellent electromagnetic compatibility.

4 Conclusion

The methanol-CVD process enables precise microstructure control in Gr-skinned SiO_2 fabric through radical manipulation and substrate engineering. Low temperatures favor C_1 species, forming defective Gr, while high temperatures enrich C_2/C_6 aromatics, producing conductive Gr. The adsorption capacity of C_1 varies significantly across different substrates. As the number of graphene layers on the SiO_2 surface increases, the adsorption energy gradually rises, making it difficult for C_1 to nucleate effectively. When the Gr layer count reaches three, the adsorption energy stabilizes, explaining the transition in SiO_2 growth from a single layer to a bilayer structure. The unique bilayer Gr structure allows for precise tuning of its electrical resistance, with the R_s of the Gr-skinned fabric being adjustable within the range of 25–150 Ω sq^{-1}. To validate its potential for integrated communication and electrothermal applications, a Gr-skinned fabric with an FSS configuration was fabricated. Band-pass FSS patterning via laser patterning enhances EMW transmittance from 3.3% to 77% while preserving Joule heating. A sandwich structure was prepared by laminating the Gr-skinned fabric with EMW transparent sheets, and the synergy between EMW transmission and Joule heating was validated. Sandwich structures maintain broadband transmission (> 60%) of 7.29 GHz and stable heating 72 °C at an applied voltage of 105 V. This work provides a scalable pathway for fabricating Gr-skinned fiber composites with electromagnetic-thermal functionality, overcoming conventional fiber limitations.

Acknowledgements This work has been supported by the National Natural Science Foundation of China (Grant No. 52222204, 52572051, 52172103, and 52231007), Fundamental Research Funds for the Central Universities (Grant No. D5000240293),

Jiangsu Provincial Program of Science and Technology (Grant No. BE2023044) and Natural Science Basic Research Program in Shaanxi (Grant No. 2022JC-25). We also thank the Analytical & Testing Center of Northwestern Polytechnical University for SEM and TEM tests.

Author Contributions Jie Liang was involved in investigation and original draft writing. Zhaochen Li and Yuchen Cao took part in investigation and visualization. Yi An assisted with software. Fang Ye and Xiaomeng Fan participated in funding acquisition, reviewing, and supervision. Qiang Song was responsible for conceptualization and writing—review.

Declarations

Conflict of interest The authors declare no interest conflict. They have no known competing financial interests or personal relationships that could have appeared to influence the work reported in this paper.

Supplementary Information The online version contains supplementary material available at https://doi.org/10.1007/s40820-026-02117-8.

References

1. Y. Wen, M. Jian, J. Huang, J. Luo, L. Qian et al., Carbonene fibers: toward next-generation fiber materials. Nano Lett. **22**(15), 6035–6047 (2022). https://doi.org/10.1021/acs.nanolett.1c04878
2. C. Chen, J. Feng, J. Li, Y. Guo, X. Shi et al., Functional fiber materials to smart fiber devices. Chem. Rev. **123**(2), 613–662 (2023). https://doi.org/10.1021/acs.chemrev.2c00192
3. Y. Qi, L. Sun, Z. Liu, Super graphene-skinned materials: an innovative strategy toward graphene applications. ACS Nano **18**(6), 4617–4623 (2024). https://doi.org/10.1021/acsnano.3c11971
4. Z. Chen, Y. Qi, X. Chen, Y. Zhang, Z. Liu, Direct CVD growth of graphene on traditional glass: methods and mechanisms. Adv. Mater. **31**(9), e1803639 (2019). https://doi.org/10.1002/adma.201803639
5. J. Liang, F. Ye, Y. Cao, R. Mo, L. Cheng et al., Defect-engineered graphene/Si_3N_4 multilayer alternating core-shell nanowire membrane: a plainified hybrid for broadband electromagnetic wave absorption. Adv. Funct. Mater. **32**(22), 2200141 (2022). https://doi.org/10.1002/adfm.202200141
6. Y. Hao, M.S. Bharathi, L. Wang, Y. Liu, H. Chen et al., The role of surface oxygen in the growth of large single-crystal graphene on copper. Science **342**(6159), 720–723 (2013). https://doi.org/10.1126/science.1243879
7. Y. Yang, H. Yuan, Y. Cheng, F. Yang, M. Liu et al., Fluid-dynamics-rectified chemical vapor deposition (CVD) preparing graphene-skinned glass fiber fabric and its application in natural energy harvest. J. Am. Chem. Soc. **146**(36), 25035–25046 (2024). https://doi.org/10.1021/jacs.4c07609
8. J. Shi, C. Yu, R. Liu, Z. Jing, X. Sun et al., Growth mechanism of graphene-skinned glass fibre fabrics driven by various carbon sources. Nano Res. **18**(9), 94907578 (2025). https://doi.org/10.26599/nr.2025.94907578
9. J. Liu, Q. Guo, H. Tian, Y. Cheng, X. Xu et al., Dimension-engineered sequential assembly of carbonene materials on arbitrary fiber substrates for electromagnetic interference shielding. Matter **8**(10), 102427 (2025). https://doi.org/10.1016/j.matt.2025.102427
10. B.J. Park, H.S. Park, Enhanced electrical conductivity of doped graphene fiber *via* vacuum deposition. Carbon Lett. **31**(4), 613–618 (2021). https://doi.org/10.1007/s42823-020-00193-3
11. G. Witjaksono, M. Junaid, M.H. Khir, Z. Ullah, N. Tansu et al., Effect of nitrogen doping on the optical bandgap and electrical conductivity of nitrogen-doped reduced graphene oxide. Molecules **26**(21), 6424 (2021). https://doi.org/10.3390/molecules26216424
12. L. Liu, J. Shi, W. Li, K. Zheng, H. Yuan et al., Rapid preparation of graphene-skinned glass fiber fabric based on propane as carbon source. Nano Res. **18**(3), 94907217 (2025). https://doi.org/10.26599/nr.2025.94907217
13. P.J. Meadows, E. López-Honorato, P. Xiao, Fluidized bed chemical vapor deposition of pyrolytic carbon–II. Effect of deposition conditions on anisotropy. Carbon **47**(1), 251–262 (2009). https://doi.org/10.1016/j.carbon.2008.10.003
14. E. López-Honorato, P.J. Meadows, P. Xiao, Fluidized bed chemical vapor deposition of pyrolytic carbon–I. Effect of deposition conditions on microstructure. Carbon **47**(2), 396–410 (2009). https://doi.org/10.1016/j.carbon.2008.10.023
15. E. López-Honorato, P.J. Meadows, P. Xiao, G. Marsh, T.J. Abram, Structure and mechanical properties of pyrolytic carbon produced by fluidized bed chemical vapor deposition. Nucl. Eng. Des. **238**(11), 3121–3128 (2008). https://doi.org/10.1016/j.nucengdes.2007.11.022
16. J. Liang, F. Ye, Q. Song, Y. Cao, S. Hui et al., In-plane heterogeneous structure-boosted interfacial polarization in graphene for wide-band and wide-temperature microwave absorption. Chem. Eng. J. **497**, 154307 (2024). https://doi.org/10.1016/j.cej.2024.154307
17. F. Ye, Q. Song, Z. Zhang, W. Li, S. Zhang et al., Direct growth of edge-rich graphene with tunable dielectric properties in

porous Si_3N_4 ceramic for broadband high-performance microwave absorption. Adv. Funct. Mater. **28**(17), 1707205 (2018). https://doi.org/10.1002/adfm.201707205

18. A. Becker, K.J. Hüttinger, Chemistry and kinetics of chemical vapor deposition of pyrocarbon: II pyrocarbon deposition from ethylene, acetylene and 1, 3-butadiene in the low temperature regime. Carbon **36**(3), 177–199 (1998). https://doi.org/10.1016/S0008-6223(97)00175-9
19. Z.P. Tang, A.J. Li, Z.W. Zhang, X. Ma, W. Wang et al., Chemistry and kinetics of heterogeneous reaction mechanism for chemical vapor infiltration of pyrolytic carbon from propane. Ind. Eng. Chem. Res. **53**(45), 17537–17546 (2014). https://doi.org/10.1021/ie5026024
20. I. Ziegler-Devin, R. Fournet, R. Lacroix, P.M. Marquaire, An interpretation of the hydrogen inhibiting effect on chemical vapor deposition of pyrocarbon. J. Anal. Appl. Pyrolysis **115**, 299–306 (2015). https://doi.org/10.1016/j.jaap.2015.08.009
21. R. Lacroix, R. Fournet, I. Ziegler-Devin, P.M. Marquaire, Kinetic modeling of surface reactions involved in CVI of pyrocarbon obtained by propane pyrolysis. Carbon **48**(1), 132–144 (2010). https://doi.org/10.1016/j.carbon.2009.08.041
22. Y. Yang, H. Yuan, M. Liu, S. Cheng, W. Li et al., Premelted-substrate-promoted selective etching strategy realizing CVD growth of high-quality graphene on dielectric substrates. ACS Appl. Mater. Interfaces **17**(4), 6825–6834 (2025). https://doi.org/10.1021/acsami.4c20313
23. Z. Qi, H. Shi, M. Zhao, H. Jin, S. Jin et al., Chemical vapor deposition growth of bernal-stacked bilayer graphene by edge-selective etching with H_2O. Chem. Mater. **30**(21), 7852–7859 (2018). https://doi.org/10.1021/acs.chemmater.8b03393
24. C. Hu, H. Li, S. Zhang, W. Li, A molecular-level analysis of gas-phase reactions in chemical vapor deposition of carbon from methane using a detailed kinetic model. J. Mater. Sci. **51**(8), 3897–3906 (2016). https://doi.org/10.1007/s10853-015-9709-2
25. K. Norinaga, O. Deutschmann, Detailed kinetic modeling of gas-phase reactions in the chemical vapor deposition of carbon from light hydrocarbons. Ind. Eng. Chem. Res. **46**(11), 3547–3557 (2007). https://doi.org/10.1021/ie061207p
26. J.M. Leyssale, J.P. Da Costa, C. Germain, P. Weisbecker, G.L. Vignoles, Structural features of pyrocarbon atomistic models constructed from transmission electron microscopy images. Carbon **50**(12), 4388–4400 (2012). https://doi.org/10.1016/j.carbon.2012.05.015
27. B. Farbos, P. Weisbecker, H.E. Fischer, J.P. Da Costa, M. Lalanne et al., Nanoscale structure and texture of highly anisotropic pyrocarbons revisited with transmission electron microscopy, image processing, neutron diffraction and atomistic modeling. Carbon **80**, 472–489 (2014). https://doi.org/10.1016/j.carbon.2014.08.087
28. C. Hu, H. Li, S. Zhang, W. Li, N. Li, Chemical vapor infiltration of pyrocarbon from methane pyrolysis: kinetic modeling with texture formation. Sci. China Mater. **62**(6), 840–852 (2019). https://doi.org/10.1007/s40843-018-9379-7
29. D. López-Díaz, M. López Holgado, J.L. García-Fierro, M.M. Velázquez, Evolution of the Raman spectrum with the chemical composition of graphene oxide. J. Phys. Chem. C **121**(37), 20489–20497 (2017). https://doi.org/10.1021/acs.jpcc.7b06236
30. H. Estrade-Szwarckopf, XPS photoemission in carbonaceous materials: a "defect" peak beside the graphitic asymmetric peak. Carbon **42**(8–9), 1713–1721 (2004). https://doi.org/10.1016/j.carbon.2004.03.005
31. J. Dong, L. Zhang, F. Ding, Kinetics of graphene and 2D materials growth. Adv. Mater. **31**(9), e1801583 (2019). https://doi.org/10.1002/adma.201801583
32. A.C. Ferrari, Raman spectroscopy of graphene and graphite: disorder, electron–phonon coupling, doping and nonadiabatic effects. Solid State Commun. **143**(1–2), 47–57 (2007). https://doi.org/10.1016/j.ssc.2007.03.052
33. A.C. Ferrari, D.M. Basko, Raman spectroscopy as a versatile tool for studying the properties of graphene. Nat. Nanotechnol. **8**(4), 235–246 (2013). https://doi.org/10.1038/nnano.2013.46
34. L.G. Cançado, A. Reina, J. Kong, M.S. Dresselhaus, Geometrical approach for the study of G′ band in the Raman spectrum of monolayer graphene, bilayer graphene, and bulk graphite. Phys. Rev. B **77**(24), 245408 (2008). https://doi.org/10.1103/physrevb.77.245408
35. L.G. Cançado, M.A. Pimenta, B.R.A. Neves, G. Medeiros-Ribeiro, T. Enoki et al., Anisotropy of the Raman spectra of nanographite ribbons. Phys. Rev. Lett. **93**(4), 047403 (2004). https://doi.org/10.1103/PhysRevLett.93.047403
36. I. Ziegler-Devin, R. Fournet, R. Lacroix, P.M. Marquaire, Pyrolysis of propane for CVI of pyrocarbon. Part IV: main pathways involved in pyrocarbon deposit. J. Anal. Appl. Pyrolysis **104**, 48–58 (2013). https://doi.org/10.1016/j.jaap.2013.09.010
37. G.L. Dong, K.J. Hüttinger, Consideration of reaction mechanisms leading to pyrolytic carbon of different textures. Carbon **40**(14), 2515–2528 (2002). https://doi.org/10.1016/S0008-6223(02)00174-4
38. W. Li, F. Liang, X. Sun, K. Zheng, R. Liu et al., Graphene-skinned alumina fiber fabricated through metalloid-catalytic graphene CVD growth on nonmetallic substrate and its mass production. Nat. Commun. **15**(1), 6825 (2024). https://doi.org/10.1038/s41467-024-51118-x
39. G. Cui, Z. Peng, Z. Liu, H. Ci, R. Liu et al., Flexible graphene@Silica fabric metasurface for electromagnetic wave absorption on high-speed aircraft. Adv. Mater. **38**(4), e16254 (2026). https://doi.org/10.1002/adma.202516254
40. M. Liu, Y. Yang, R. Liu, K. Wang, S. Cheng et al., Carbon nanotubes/graphene-skinned glass fiber fabric with 3D hierarchical electrically and thermally conductive network. Adv. Funct. Mater. **34**(49), 2409379 (2024). https://doi.org/10.1002/adfm.202409379
41. C.-Z. Qi, P. Min, X. Zhou, M. Jin, X. Sun et al., Multifunctional asymmetric bilayer aerogels for highly efficient electromagnetic interference shielding with ultrahigh electromagnetic wave absorption. Nano-Micro Lett **17**(1), 291 (2025). https://doi.org/10.1007/s40820-025-01800-6
42. Y. Zhou, W. Zhang, D. Pan, Z. Li, B. Zhou et al., Absorption-reflection-transmission power coefficient guiding gradient

distribution of magnetic MXene in layered composites for electromagnetic wave absorption. Nano-Micro Lett. **17**(1), 147 (2025). https://doi.org/10.1007/s40820-025-01675-7

43. Q. Wei, S. Pei, X. Qian, H. Liu, Z. Liu et al., Superhigh electromagnetic interference shielding of ultrathin aligned pristine graphene nanosheets film. Adv. Mater. **32**(14), 1907411 (2020). https://doi.org/10.1002/adma.201907411
44. Y. Xie, S. Liu, K. Huang, B. Chen, P. Shi et al., Ultra-broadband strong electromagnetic interference shielding with ferromagnetic graphene quartz fabric. Adv. Mater. **34**(30), e2202982 (2022). https://doi.org/10.1002/adma.202202982
45. Y. Cao, F. Ye, J. Liang, L. Qi, R. Mo et al., Structural-functional-integrated ultra-wideband microwave-absorbing composites based on in situ-grown graphene meta-nanointerface. Adv. Funct. Mater. **34**(52), 2411271 (2024). https://doi.org/10.1002/adfm.202411271
46. F. Costa, A. Monorchio, A frequency selective radome with wideband absorbing properties. IEEE Trans. Antennas Propag. **60**(6), 2740–2747 (2012). https://doi.org/10.1109/TAP.2012.2194640
47. M. Xiao, L. Zhang, J. Li, L. Chen, J. Sun et al., Thermal sintering matchability between low-temperature cofired ceramic substrate and silver pastes and the effect of CuO on silver diffusion inhibition. Adv. Eng. Mater. **26**(7), 2301901 (2024). https://doi.org/10.1002/adem.202301901
48. H. Chen, Y.-C. Hsu, E. Zhai, R. Bahrami, M.-H. Lee et al., Copper-coated carbon fiber composites for electromagnetic interference shielding applications. Appl. Surf. Sci. **702**, 163392 (2025). https://doi.org/10.1016/j.apsusc.2025.163392
49. K. Wang, X. Li, H. Fan, S. Xiong, B. Liu et al., Preparation of conductive silver paste with mixed nanostructured silver powders. J. Mater. Eng. Perform. **34**(11), 9645–9653 (2025). https://doi.org/10.1007/s11665-025-10766-w
50. Y. Huang, Y. Wang, L. Gao, X. He, P. Liu et al., Characterization of stretchable SWCNTs/Lycra fabric electrode with dyeing process. J. Mater. Sci. Mater. Electron. **28**(5), 4279–4287 (2017). https://doi.org/10.1007/s10854-016-6051-7
51. J. Cao, Z. Zhang, H. Dong, Y. Ding, R. Chen et al., Dry and binder-free deposition of single-walled carbon nanotubes on fabrics for thermal regulation and electromagnetic interference shielding. ACS Appl. Nano Mater. **5**(9), 13373–13383 (2022). https://doi.org/10.1021/acsanm.2c03035
52. J.L. Carter, C.A. Kelly, J.E. Marshall, M.J. Jenkins, Effect of thickness on the electrical properties of PEDOT: PSS/Tween 80 films. Polym. J. **56**(2), 107–114 (2024). https://doi.org/10.1038/s41428-023-00854-w

 https://doi.org/10.1007/s40820-026-02117-8